PROCEEDINGS, 46th Workshop on Geothermal Reservoir Engineering
Stanford University, Stanford, California, February 15-17, 2021
SGP-TR-218

The DInSAR Analysis with Machine Learning for Delineating Geothermal Sites at the Brady Geothermal Field

Mahmut Cavur[1], Jim Moraga[2], H. Sebnem Duzgun[2], Hilal Soydan[2] and Ge Jin[3]

[1] Management Information System Department, Kadir Has University, İstanbul, Turkey,

[2] Mining Engineering Department, Colorado School of Mines, Golden, CO 80401, USA,

[3] Department of Geophysics, Colorado School of Mines, Golden, CO 80401, USA,

mahmut.cavur@khas.edu.tr

Keywords: Displacement on Geothermal, K-Means, DInSAR, Deformation on Brady, Unsupervised classification.

ABSTRACT

The availability of high temporal resolution and different types of data acquired with advanced SAR techniques allow researchers to compute and analyze the displacement values in a region of interest for various purposes accurately and cost-effectively. In line with that, geothermal activities, such as production and injection operations, create direct and indirect deformations in and around the geothermal area that are in the form of subsidence or uplift movements. These movements are also strongly related to the structural geology of the site. To this end, identifying deformation patterns and understanding their temporal and spatial changes provides invaluable information that can be related to the operational activities in the geothermal site to characterize the geothermal reservoir and understand the operational impacts in the region. In this study, we present the machine learning algorithms integrated with Differential Interferometric Synthetic Aperture Radar (DInSAR) technique to delineate subsidence and uplift movements in the Brady Geothermal Site located in Nevada. For this purpose, we used DInSAR to identify vertical displacements in millimetric accuracy with a pair of Sentinel-1A SAR data (Jan.10th & Dec.24th, 2019). Then, we implemented K-means clustering as the machine learning algorithm to delineate the patterns of movements in the geothermal field and to compare the identified classes with earlier studies. According to the findings, average displacement was calculated as 9 mm/year while the maximum subsidence and maximum uplift were measured as -13 mm/year and 21 mm/yr, respectively. For validation purposes, The DInSAR results are compared and verified with earlier studies focusing on displacement trends for Brady's geothermal site. We apply the k-means algorithm for the validation of patterns created by geothermal activities. Besides, the visual investigation of the spatial distribution of subsidence and uplift reveals that the calculated deformation patterns overlap with the wells' distribution, fault zone, and geothermal activities in the region, pointing out the operational sequences in the site. The findings indicate the usability of the k-means clustering algorithm to highlight and enclose the deformation clusters closely related to geothermal activities.

1. INTRODUCTION

Delineating the geothermal fields using the displacements caused by the operational factors plays a critical role in understanding the nature of the operation and the reservoir behavior. Interferometric Synthetic Aperture Radar (InSAR) provides a reliable and cost-effective method for monitoring the geothermal sites using satellite images (e.g., Sentinel 1, Radarsat, ERS SAR). Researchers have been developing new algorithms such as Differential Synthetic Aperture Radar Interferometry (DInSAR) (Gabriel et al., 1989), SqueeSAR (Raspini et al., 2015), Small Baseline Subset Interferometry (SBAS) (Berardino et al., 2002), and Persistent Scatterer Interferometry (PSI) (M. Crosetto et al., 2016) that can be applied on radar data to analyze deformation caused by natural processes (e.g., landslides) and human-made operations (e.g., geothermal operations). Geothermal operations cause displacement with low velocities (e.g. (Cavur et al., 2021; Ali et al., 2016; Reinisch et al., 2020)), therefore, analysis of displacements using satellite images requires sophisticated algorithms (e.g. (Colesanti & Wasowski, 2006; Cigna et al., 2019; Tomás et al., 2016)). The implementation of these algorithms on the Brady Geothermal field, Nevada-USA are (Ali et al., 2016; Cavur et al., 2021), Landau-Germany (Heimlich et al., 2015), Euhanean-Italy (Strozzi et al., 2000), Marangin Jambi-Indonesia (Nouban & Abazid, 2017), Cerro Prieto and Heber-USA (Mellors et al., 2018), and Acoculco-Mexico (Cigna et al., 2019). The majority of these works focus on identifying the amount of displacement and velocity of the movements for a given period of time. The type, direction, magnitude, and speed of displacement in the geothermal fields depend on the operational and reservoir characteristics. Due to the slow-motion displacement characteristics of the geothermal fields analyzing the pattern of the displacement with its magnitude and velocity have great potential to obtain insight into the behavior of the geothermal field over time.

In this study, we proposed the use of the DInSAR algorithm coupled with a machine learning (ML) method, namely, K-Means clustering, to analyze and monitor the Brady geothermal field in order to delineate the pattern of ground displacements created by the geothermal operations. Then we compared and verified the results with earlier studies. This allowed us to evaluate and discuss the relationship between displacement patterns and geothermal operations.

2. THE STUDY AREA AND DATA

The study area of the Brady geothermal field is located 80 km east-northeast of Reno, Nevada (Figure 1). The site has been functional since 1992 generating power of 15 megawatts. There are three injection wells (located at the Northeast) and six production wells (located at the Southwest) in the field. The human-made structures and buildup in the Area of Interest (AOI) are indicated in Figure 1. The predominant fault system and well's injection direction are north-northeast (NNE), which is very common to observe such fault systems on geothermal sites. The previous studies that have been carried out on the Brady geothermal field indicated a correlation between subsidence and operations, which concentrated on the fault zone (Ali et al., 2016). Ali et al., (2016) provide reasons for the deformations as thermal cooling of the reservoir, the compaction of the sedimentary layers, and the disturbance of the equilibrium between the fluids and reactive minerals. Hence, analysis of deformation patterns could provide insight into the understanding role of factors causing these patterns.

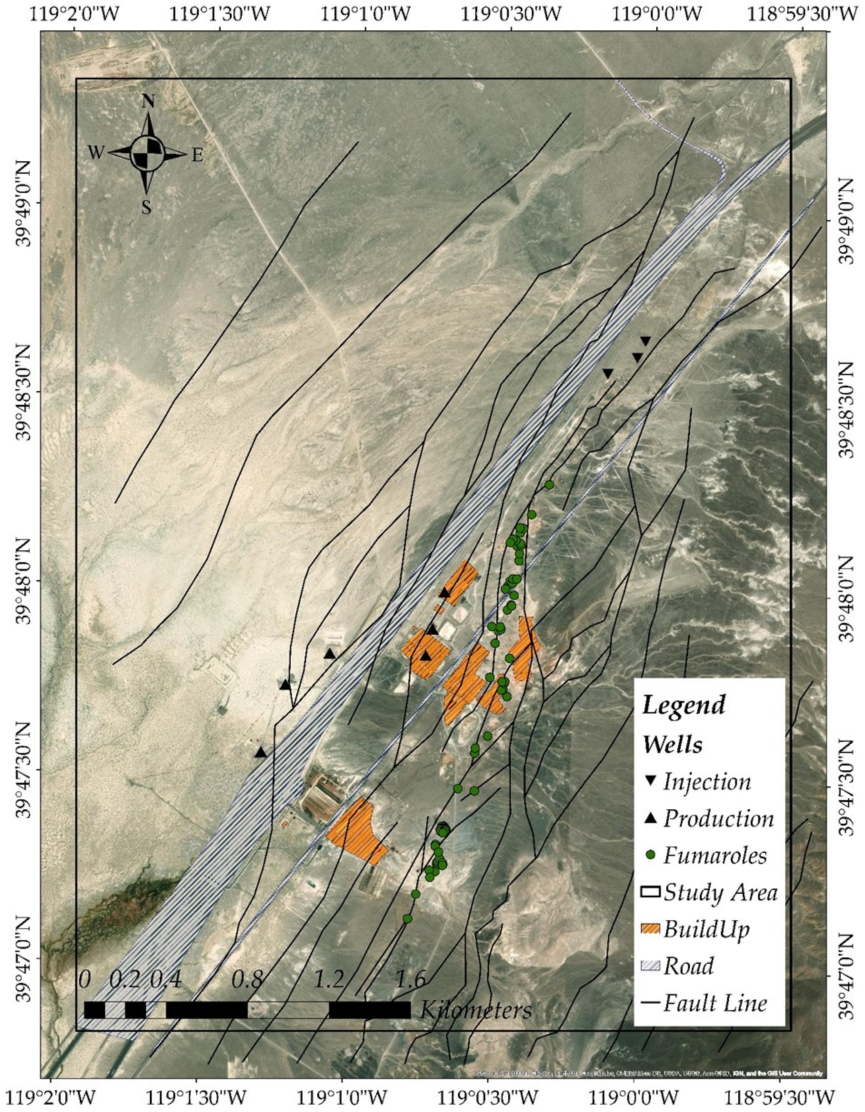

Figure 1: The area of interest defined for the Brady geothermal field.

The European Space Agency (ESA) has provided Sentinel 1 SAR data for free through the COPERNICUS Programme since 2014. The Sentinel 1 satellites follow a 12-day cycle of 175 orbits per cycle, and the SAR data can be found from https://scihub.copernicus.eu. Sentinel-1 data has a 250 km x 180 km wide range and 5 m x 20 m spatial resolution with three swaths containing nine bursts each (Figure 2). InSAR data has X, C, S, L, and P bands in wide wavelengths (1mm to 1m); high frequencies (0.3 to 300 GHz); dual-polarization (VV+VH and HH+HV), which helps to understand the structure of the earth surface penetrating clouds, rain, water, ground (Singh Virk et al., 2018).

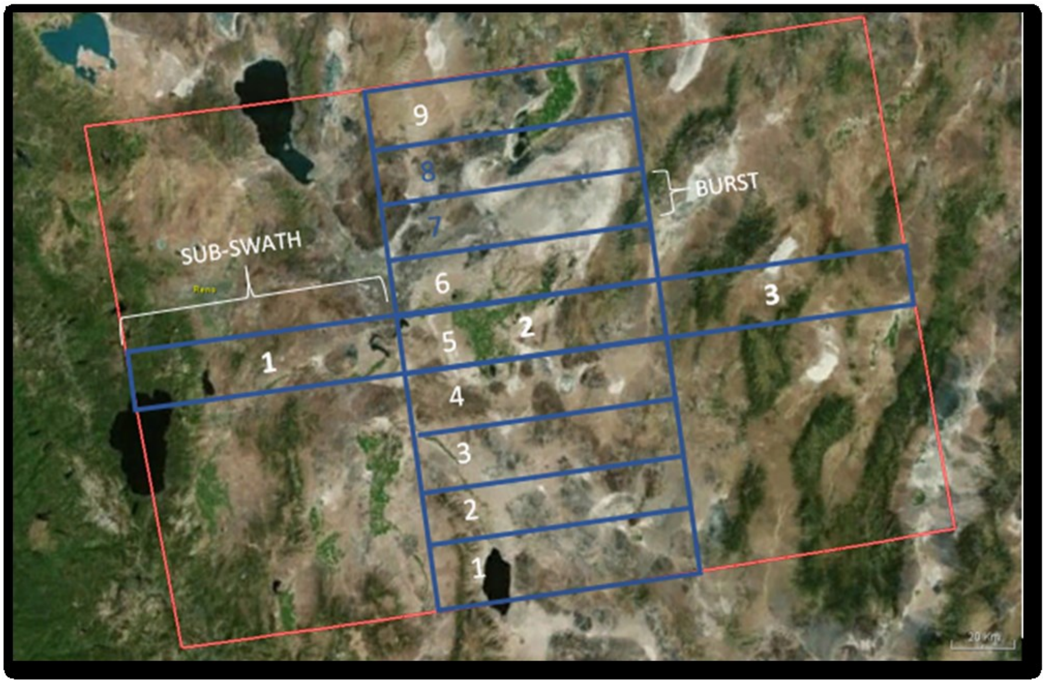

Figure 2: Interferometric Wide Single Look Complex Bursts and Sub-Swaths.

In this study, we used SAR 1A images with IW SLC C-band. We preferred to use VV polarization since it was suggested from the previous studies (Vaka et al., 2017). Specifically, we adopted 7 and 8 bursts of the 2nd sub-swath for AOI. The phase contribution of the SAR data has been used for the displacement analysis and error correction in this site. We selected two images from 2019 for the DInSAR analysis (Table 1).

Table 1. Dataset used for DInSAR Analysis.

Period (yyyy-mm-dd)	Days	Master Scene Acquisition Date (yyyy-mm-dd)	Track	Pass	Number of Images
2019-01-10 AND 2019-12-24	348	2019-12-24	144	Descending	2

The orbital file, atmospheric data, and DEM creation for related data have been downloaded online in real-time while processing data.

3. ANALYSIS OF DISPLACEMENTS

The methodology consists of two main steps which are “DInSAR Displacement Analysis” and “Extraction of Displacements Patterns Using K-Means Clustering”. The main logic behind each step were explained in the following subsections.

3.1. DInSAR Displacement Algorithm

Synthetic Aperture Radar (SAR) is a microwave imaging system penetrating the cloud, the water providing day and night imaging capabilities. It carries amplitude and phase information obtained from the back starred microwave signals from the ground, rocks, buildings, and vegetation, etc.

The interferometric phase of SAR data has the following contributions (Fárová et al., 2019):

$$\Delta\varphi = \Delta\varphi_{flat} + \Delta\varphi_{height} + \Delta\varphi_{displacement} + \Delta\varphi_{atmosphere} + \Delta\varphi_{noise} \tag{1}$$

where $\Delta\varphi_{flat}$ is the phase contribution of the flat earth, $\Delta\varphi_{height}$ indicates topography $\Delta\varphi_{displacement}$ is displacement in Line-Of-Sight (LOS), $\Delta\varphi_{atmosphere}$ is the delay of radar wave propagation through the atmosphere and $\Delta\varphi_{noise}$ is the residual noise.

DInSAR displacement result is in LOS, which is called slant-range direction; and should be converted in a vertical direction by using the following Equation 2.

$$vert\_disp = (\phi_{unw} . \lambda) / (-4\pi(cos\theta_{inc})) \tag{2}$$

where ϕ_{unw} is the unwrapped phase, λ is the radar wavelength, and θ_{inc} is the incidence angle.

DInSAR algorithm uses the phase contribution of the SAR data, which is suited for the long-term and slow surface deformation analysis (Carnec & Delacourt, 2000; Raspini et al., 2017). For this purpose, a pair of SAR images at different times for the same area is needed to create an interferometric result for further analysis in the DInSAR. The interferogram is the image containing the measurements of the phase difference of two images taken for the same area at different times. Although several values contribute to the phase, the DInSAR technique only accounts for $\Delta\varphi_{displacement}$ contribution and removes the rest of the contribution in Equation 1.

The coherence between data should be as high as possible to get an accurate and reliable result. Since the result of the analysis depends on two image quality, forested, vegetated, snow-covered areas, and moisture changes have an impact on the coherence between image pairs. Although the technique has been used for only one contribution of the phase, it is widely used for slow subsidence/uplift movements successfully (Fárová et al., 2019; Mouratidis & Costantini, 2013; M. Crosetto et al., 2017).

The flowchart of implementing the DInSAR technique is shown in Figure 3.

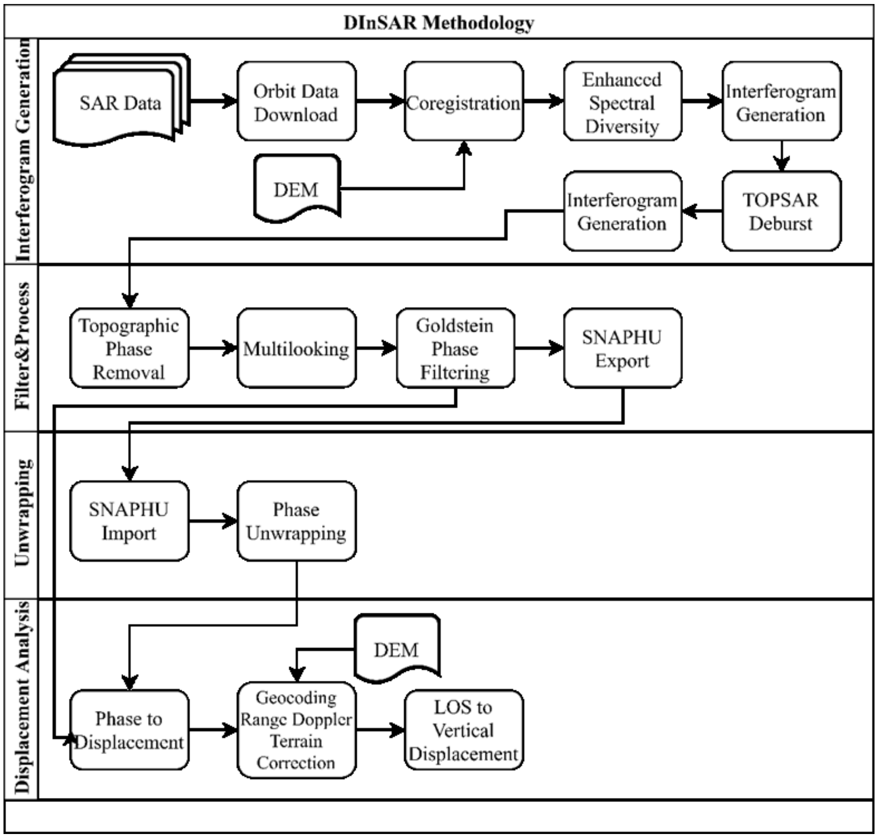

Figure 3: Flowchart of the DInSAR Method used for the analysis of displacements in the Brady geothermal field.

The method of the DInSAR can be divided into four main parts:

- Data Preparation and Interferogram Generation
- Filter and Process
- Unwrapping of Interferograms
- Displacement Calculation and Visualization

As shown in Figure 2, the data provided by ESA has three swaths and 9 bursts for each image. Therefore, the swath and burst should be selected and split for the AOI. The orbital files need to be downloaded, and DEM should be created for the interferogram generation. The product of the first phase will be interferograms, which is the phase difference of the image pairs.

In the second step, several filtering operations and topography removal are applied to the interferograms. Multi-looking improves the image quality by reducing the speckle and resampling pixels into a square image. Moreover, Goldstein phase filtering helps to filter the phase noise preserving the fringe edge (Feng et al., 2016).

The third step is called the unwrapping process. Since generated interferograms are in radians, the statistical-cost and network-flow (Chen & Zebker, 2001) algorithm is used by SNAPHU, which is a freely available software unwrapping to convert the value into mm.

The final phase of the operation is to calculate the displacement of the image pairs from Equation 2 in the vertical direction. Then, the result is visualized after Range Doppler terrain correction that orthorectifies the result. Finding a stable point after terrain correction is essential to re-calculate the displacement values on the rest of the pixels. Finally, several basic post-processing methods (georeferencing, resampling, extending, re-calculation of displacement pixels, etc.) are applied using GIS software for visualization, re-calculation, and reporting. We used SNAP software, which is freely available and developed especially for Sentinel data analysis by ESA for the DinSAR.

3.2.Extraction of Displacements Patterns Using K-Means Clustering

Analysis of clusters is an unsupervised machine learning (ML) method used for pattern analysis considering similarity matrics. The K-Means algorithm is one of the most well-known algorithms used for clustering. It divides objects into clusters (Li & Wu, 2012). We adopted this algorithm in this study for analyzing the pattern of the displacements. The first step in K-Means is to calculate the k centroids. In the second step, the nearest centroid location for each pixel is found by using s the distance metrics. Briefness, efficiency, and celerity are the main reasons to use K-means clustering. (Dhanachandra et.al., 2015). Appendix A shows the K-means clustering algorithm developed on R Script in this study.

4. RESULTS AND DISCUSSION

DInSAR results (Figure 4) for Brady geothermal field indicate the presence of the subsidence and uplift in the AOI as expected. The highest subsidence detected in the AOI is -13 mm/yr whereas the highest uplift detected is 21 mm/yr. The average displacement of the field in the AOI is 9 ± 6 mm/yr. As shown in Figure 4, subsidence occurred mainly around production wells, which are located in the middle of the geothermal field. On the other hand, the uplift occurred around the injection wells, which are located in the North East (NE) of the geothermal field. This validates that operations in the field create a displacement in the middle of the field as expected and reported in earlier studies. In addition to that, the subsidence correlated with the fault zone shown in Figure 2 (Mellors et al., 2018). It is clear that the pattern of subsidence overlaps with the alignment of the fault zones in the geothermal field.

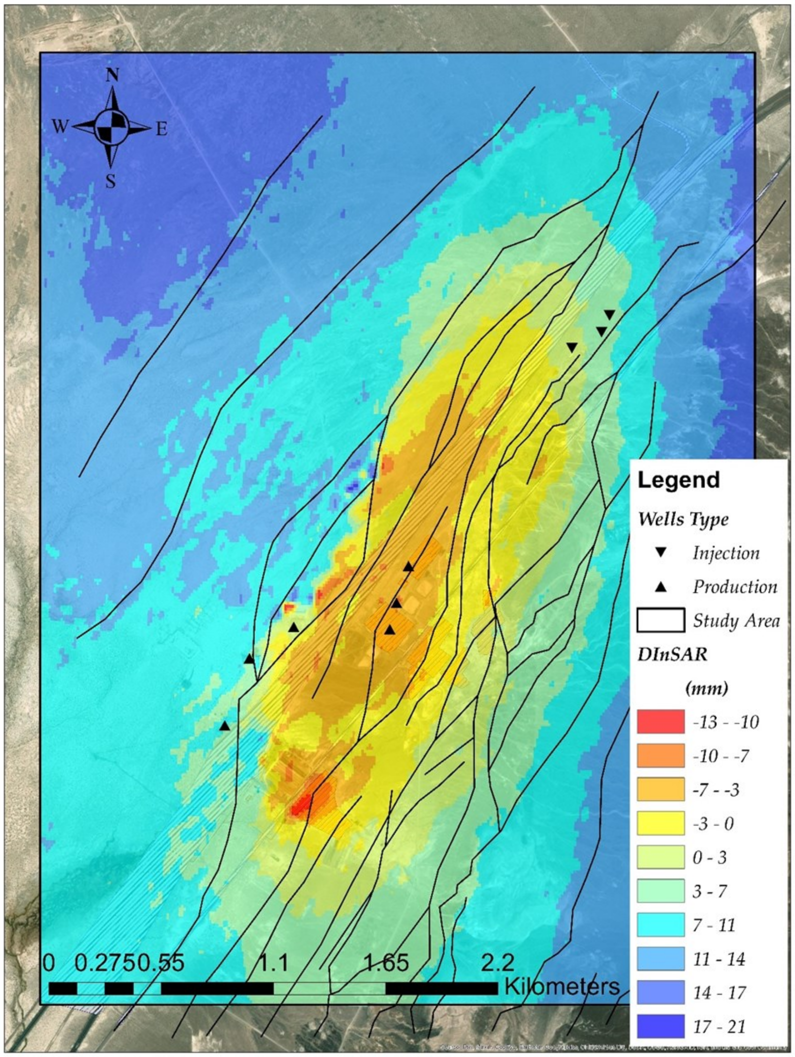

Figure 4: The DInSAR Analysis Result for Brady Field.

As shown in Figure 5, cluster 1 (given in red color in Figure 5) concentrated in the center of the AOI whereas the uplift has a pattern around the subsidence as an oval ring pattern and has intensity on the north-northeast (NNE) part of the AOI. The three injection wells were located on the uplift clusters whereas the production wells were located on the subsidence field in the middle (Figure 5).

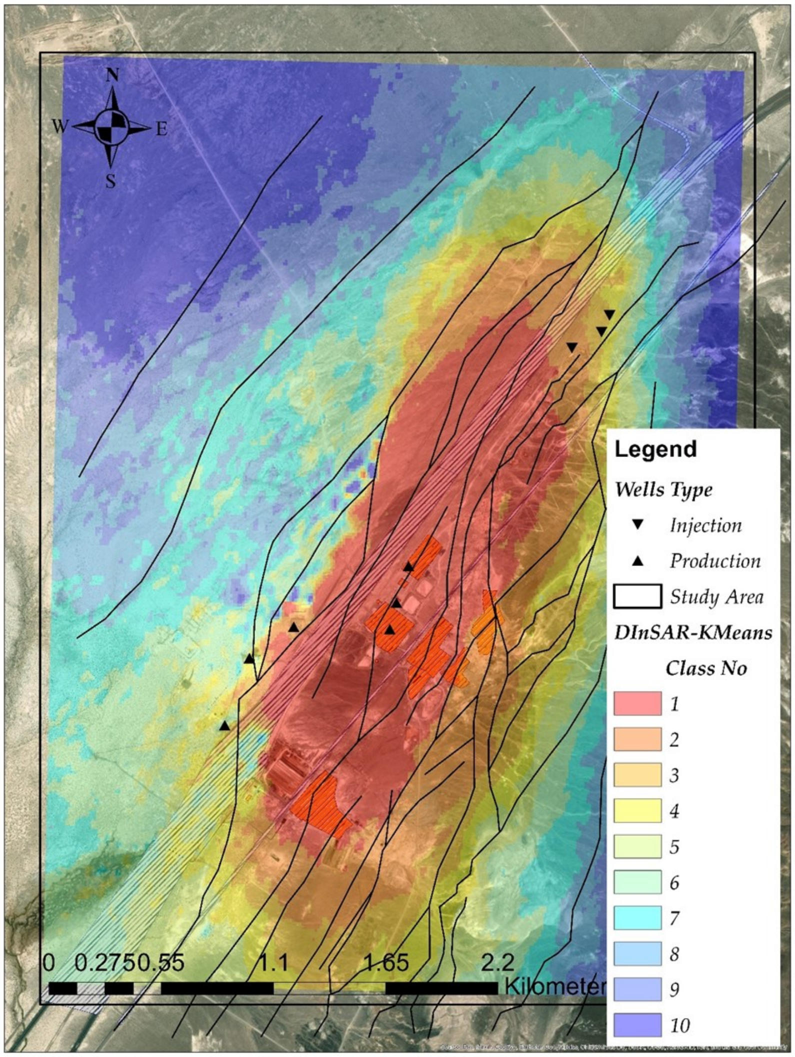

Figure 5: The K-Means results with ten clusters.

Table 2 shows the average displacements and the number of pixels in each center. Clusters 1 and 2 had negative values indicating subsidence and were shown in red and orange in Figure 5. Production wells are located in these two clusters whereas the injection wells are located in uplift clusters, which are shown in clusters 3 and 4.

Table 2. Cluster Statistics for DInSAR.

	C1	C2	C3	C4	C5	C6	C7	C8	C9	C10
Disp(mm/yr)	-4.91	-2.13	0.52	3.58	6.16	8.26	9.97	11.60	13.28	14.72
# of Pixels	839	981	832	1145	1670	2444	2578	2636	2398	2745

The Brady geothermal field has recently been studied by several researchers (Ali et al., 2016; Mellors et al., 2018; Reinisch, et al., 2018). We compared the results with earlier studies for validation. Table 3 shows the comparison of the earlier studies with the findings of this study. The direction of displacements given by (Reinisch et al., 2018) and (Cavur et al., 2021) are similar to the results of this study, where the displacements are oriented in NNE. The average deformation values may change due to the use of different time periods. As a result, the deformation analysis of 2019 provided in this study is satisfactory as they are inline with the findings of the two different research studies, even though each study used different algorithms and software tools. The maximum subsidence obtained from DInSAR analyses was approximately -13 mm/yr in the AOI, whereas uplift values are around 21 mm/yr.

Table 3. Comparison of the Earlier Studies with Our Analysis Result.

Imgs	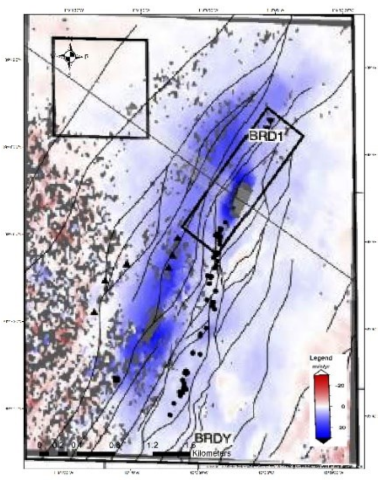	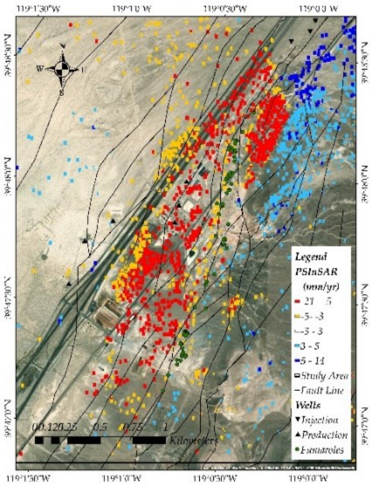	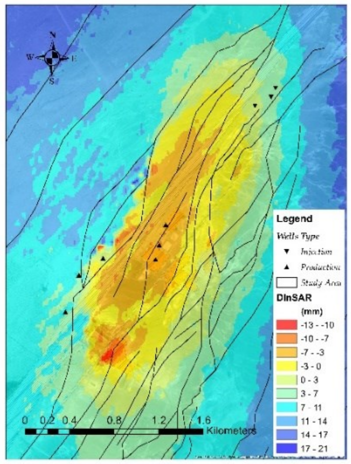
Time	a) 2016 July to 2017 Aug	b) 2017 Jan to 2019 Dec	c) 2019 Jan and 2019 Dec
Range	-25 - +25	-21 - +11	-13 - +21
Stdv.	± 3.3	± 4.65	± 6
Avg.	-9.9	- 1.22	9
Ref.	(Reinisch et al., 2018)	(Cavur et al., 2021)	DInSAR analysis results in this study

(**Abbreviations**: Imgs: Images - Avg: Average - Stdv: Standart Devaiton – Ref: Reference)

5. CONCLUSION

In this study, both DInSAR and K-Means algorithms have been implemented on one of the well-known geothermal field (the Brady geothermal field) to reveal the pattern of displacements that may provide insight into the effects of the operations. The obtained results are compatible with the previous studies concerning the direction and pattern of the displacement. This study proves that DInSAR analyses coupled with ML algorithms can be a useful tool for monitoring geothermal fields, which have deformations in slow-motion. The range of the subsidence and average displacement with standard deviation is -13 – 21 mm/yr and 9 ± 6 mm/yr, respectively. We also demonstrated that the clusters obtained from the K-means algorithm clearly define the subsidence and uplift patterns in the geothermal field. The expected subsidence area and its direction should be similar every year if there are no extraordinary changes in the AOI like a landslide or natural hazard. The former studies conducted on the same site in different years with different techniques prove that the pattern of the subsidence remains the same for the Brady geothermal field. It is important to verify these analyses with the ground truth. Besides, the relation of different operational practices in the field should be investigated in further research. The authors plan to extend their research in this direction.

ACKNOWLEDGMENTS

Acknowledgments: We thank the US Department of Energy DOE-EERE – Geothermal Technologies Program for funding this work within the project DE- EE0008760 entitled `Detection of Potential Geothermal Exploration Sites from Hyperspectral Images via Deep Learning`. We are grateful to Dr. Curtis W. Chen and Dr. Howard A. Zebker for providing Snaphu for free to researchers. We appreciate the European Space Agency (ESA) for making Synthetic Aperture Radar data from the Sentinel satellite missions available to this work.

APPENDIX A

The R code for the K-Means Algorithm

```
# k-means for one layer, no distance
# r_pts: is a data frame with x, y coordinates
# img_name: name of the layer (data frame column), to analyze
kmeans_tmp <- function(r_pts, img_name, n_clusters=5, plot_image = FALSE) {
  pt_tmp_dst <- r_pts[,c(img_name)]
  k_tmp_dst_pt<- r_pts[,c("x","y")]
  center = mean(pt_tmp_dst)
  scale = sd(pt_tmp_dst)
  pt_tmp_dst<-(pt_tmp_dst-mean(pt_tmp_dst))/(sd(pt_tmp_dst))
  set.seed(42)
  k_tmp_dst <- kmeans(pt_tmp_dst,n_clusters, iter.max = 2000)
  cluster_lst <- as.data.frame(k_tmp_dst$centers)
  cluster_lst$cluster <- seq(1,length(k_tmp_dst$centers))
  colnames(cluster_lst)<-c("temp", "cluster")
  sorted_clusters <- cluster_lst[order(cluster_lst[,1]),]
  k_tmp_dst$cluster <- match(unlist(k_tmp_dst$cluster), sorted_clusters[,2])
  k_tmp_dst$centers <- unlist(sorted_clusters$temp)
  k_tmp_dst$size <- k_tmp_dst$size[sorted_clusters$cluster]
  k_tmp_dst$withinss <- k_tmp_dst$withinss[sorted_clusters$cluster]
  k_tmp_dst$center <- center
  k_tmp_dst$scale <- scale
  k_tmp_dst$centroids <- k_tmp_dst$centers*k_tmp_dst$scale+k_tmp_dst$center
  if (plot_image){
    k_tmp_dst_pt[,3] <- k_tmp_dst$cluster
    coordinates(k_tmp_dst_pt) <- ~ x+ y
    proj4string(k_tmp_dst_pt) <- crs(" +proj=utm +zone=11 +datum=WGS84 +units=m +no_defs +ellps=WGS84 +towgs84=0,0,0 ")
    gridded(k_tmp_dst_pt) <- TRUE
    plot(k_tmp_dst_pt, col=rev(rainbow(n_clusters)), main=img_name)
    return(k_tmp_dst_pt)
  }
  return (k_tmp_dst) }
```

REFERENCES

Ali, S. T., Akerley, J., Baluyut, E. C., Cardiff, M., Davatzes, N. C., Feigl, K. L., Foxall, W., Fratta, D., Mellors, R. J., Spielman, P., Wang, H. F., & Zemach, E. (2016). Time-series analysis of surface deformation at Brady Hot Springs geothermal field (Nevada) using interferometric synthetic aperture radar. Geothermics, 61, 114–120. https://doi.org/10.1016/j.geothermics.2016.01.008

Berardino, P., Fornaro, G., Lanari, R., Member, S., Sansosti, E., & Member, S. (2002). A New Algorithm for Surface Deformation Monitoring Based on Small Baseline Differential SAR Interferograms. 40(11), 2375–2383.

Carnec, C., & Delacourt, C. (2000). Three years of mining subsidence monitored by SAR interferometry, near Gardanne, France. European Space Agency, (Special Publication) ESA SP, 478, 141–149.

Cavur, M., Moraga, J., Duzgun, H. S., Soydan, H., & Jin, G. (2021). Displacement Analysis of Geothermal Field Based on PSInSAR And SOM Clustering Algorithms A Case Study of Brady Field, Nevada—USA. Remote Sensing, 13(3), 349. https://doi.org/https://doi.org/10.3390/rs13030349

Chen, C. W., & Zebker, H. A. (2001). Two-dimensional phase unwrapping with the use of statistical models for cost functions in nonlinear optimization. 18(2), 338–351.

Cigna, F., Tapete, D., Garduño-Monroy, V. H., Muñiz-Jauregui, J. A., García-Hernández, O. H., & Jiménez-Haro, A. (2019). Wide-area InSAR survey of surface deformation in urban areas and geothermal fields in the eastern Trans-Mexican Volcanic Belt, Mexico. Remote Sensing, 11(20), 1–33. https://doi.org/10.3390/rs11202341

Colesanti, C., & Wasowski, J. (2006). Investigating landslides with space-borne Synthetic Aperture Radar (SAR) interferometry. Engineering Geology, 88(3–4), 173–199. https://doi.org/10.1016/j.enggeo.2006.09.013

Crosetto, M, Monserrat, O., Barra, A., & Crippa, B. (2017). Deformation Measurement Using Sentinel-1a / B Imagery. XLII(September), 597–600.

Crosetto, M, Monserrat, O., Cuevas-González, M., Devanthéry, N., & Crippa, B. (2016). Persistent Scatterer Interferometry: A review. ISPRS Journal of Photogrammetry and Remote Sensing, 115, 78–89. https://doi.org/10.1016/j.isprsjprs.2015.10.011

Dhanachandra, N., Manglem, K., & Chanu, Y. J. (2015). Image Segmentation Using K-means Clustering Algorithm and Subtractive Clustering Algorithm. Procedia Computer Science, 54, 764–771. https://doi.org/10.1016/j.procs.2015.06.090

Fárová, K., Jelének, J., Kopačková-Strnadová, V., & Kycl, P. (2019). Comparing DInSAR and PSI Techniques Employed to Sentinel-1 Data to Monitor Highway Stability: A Case Study of a Massive Dobkoviˇcky Landslide, Czech Republic. Czech Geological Survey, 1–23. https://doi.org/10.3390/rs11222670

Feng, Q., Xu, H., Wu, Z., You, Y., Liu, W., & Ge, S. (2016). Improved Goldstein interferogram filter based on local fringe frequency estimation. Sensors (Switzerland), 16(11), 1–17. https://doi.org/10.3390/s16111976

Gabriel, A. K., Goldstein, R. M., & Zebker, H. A. (1989). Mapping small elevation changes over large areas: differential radar interferometry. Journal of Geophysical Research, 94(B7), 9183–9191. https://doi.org/10.1029/JB094iB07p09183

Heimlich, C., Gourmelen, N., Masson, F., Schmittbuhl, J., Kim, S. W., & Azzola, J. (2015). Uplift around the geothermal power plant of Landau (Germany) as observed by InSAR monitoring. Geothermal Energy, 3(1), 1–12. https://doi.org/10.1186/s40517-014-0024-y

Li, Y., & Wu, H. (2012). A Clustering Method Based on K-Means Algorithm. Physics Procedia, 25, 1104–1109. https://doi.org/10.1016/j.phpro.2012.03.206

Mellors, R. J., Xu, X., Matzel, E., Sandwell, D., & Fu, P. (2018). New Potential of InSAR for Geothermal Systems. 43rd Workshop on Geothermal Reservoir Engineering, 1–4.

Mouratidis, A., & Costantini, F. (2013). PS and SBAS Interferometry Over the Broader Area Of Thessaloniki, Greece, Using The 20-Year Archive Of ERS And Envisat Data. 2011(January 2012), 19–23.

Nouban, F. and Abazid, M. (2017). Plastic degrading fungi Trichoderma viride and Aspergillus nomius isolated from local landfill soil in Medan, Iopscience.Iop. Org, 8(February. Iopscience.Iop. Org, 8(February 2018), 68–74. https://doi.org/10.1088/1755-1315

Raspini, F., Ciampalini, A., Conte, S. Del, Lombardi, L., Nocentini, M., Gigli, G., Ferretti, A., & Casagli, N. (2015). Exploitation of Amplitude and Phase of Satellite SAR Images for Landslide Mapping: The Case of Montescaglioso (South Italy). November. https://doi.org/10.3390/rs71114576

Reinisch, E. C., Cardiff, M., & Feigl, K. L. (2018). Characterizing volumetric strain at Brady Hot Springs, Nevada, the USA using geodetic data, numerical models, and prior information. Geophysical Journal International, 215(2), 1501–1513. https://doi.org/10.1093/GJI/GGY347

Reinisch, E. C., Cardiff, M., Kreemer, C., Akerley, J., & Feigl, K. L. (2020). Time-Series Analysis of Volume Change at Brady Hot Springs, Nevada, USA, Using Geodetic Data From 2003–2018. Journal of Geophysical Research: Solid Earth, 125(9), 1–18. https://doi.org/10.1029/2019JB017816

Singh Virk, A., Singh, A., & Mittal, S. K. (2018). Advanced MT-InSAR Landslide Monitoring: Methods and Trends. Journal of Remote Sensing & GIS, 07(01), 1–6. https://doi.org/10.4172/2469-4134.1000225

Strozzi, T., Tosi, L., Carbognin, L., Wegmüller, U., & Galgaro, A. (2000). Monitoring Land Subsidence in the Euganean Geothermal Basin with Differential SAR Interferometry. European Space Agency, (Special Publication) ESA SP, 478, 167–176.

Tomás, R., Li, Z., Lopez-Sanchez, J. M., Liu, P., & Singleton, A. (2016). Using wavelet tools to analyze seasonal variations from InSAR time-series data: a case study of the Huangtupo landslide. Landslides, 13(3), 437–450. https://doi.org/10.1007/s10346-015-0589-y

Vaka, D. S., Sharma, S., & Rao, Y. S. (2017). Comparison of HH and VV Polarizations for Deformation Estimation using Persistent Scatterer Interferometry. 38th Asian Conference on Remote Sensing - Space Applications: Touching Human Lives, ACRS 2017, 2017-October.